

## Polytetrafluoroethylene (PTFE) Lubrication of Rolling Point Contacts by Double Transfer Films: Relationships between Friction and Lubricant Film Distribution Revealed by Spacer Layer Imaging and Molecular Dynamics

Thomas Reichenbach, Stephan von Goedel, Stefan Peeters, Georgios Vokolos, Florian König, Georg Jacobs, Gianpietro Moras & Michael Moseler

To cite this article: Thomas Reichenbach, Stephan von Goedel, Stefan Peeters, Georgios Vokolos, Florian König, Georg Jacobs, Gianpietro Moras & Michael Moseler (2025) Polytetrafluoroethylene (PTFE) Lubrication of Rolling Point Contacts by Double Transfer Films: Relationships between Friction and Lubricant Film Distribution Revealed by Spacer Layer Imaging and Molecular Dynamics, Tribology Transactions, 68:5, 1102-1113, DOI: [10.1080/10402004.2025.2513933](https://doi.org/10.1080/10402004.2025.2513933)

To link to this article: <https://doi.org/10.1080/10402004.2025.2513933>



© 2025 The Author(s). Published with license by Taylor & Francis Group, LLC.



Published online: 18 Sep 2025.



Submit your article to this journal [↗](#)



Article views: 227



View related articles [↗](#)



View Crossmark data [↗](#)

# Polytetrafluoroethylene (PTFE) Lubrication of Rolling Point Contacts by Double Transfer Films: Relationships between Friction and Lubricant Film Distribution Revealed by Spacer Layer Imaging and Molecular Dynamics

Thomas Reichenbach<sup>a,\*</sup> , Stephan von Goedel<sup>b,\*</sup> , Stefan Peeters<sup>a,c</sup> , Georgios Vokolos<sup>b</sup>, Florian König<sup>b</sup> , Georg Jacobs<sup>b</sup> , Gianpietro Moras<sup>a</sup> , and Michael Moseler<sup>a,c,d</sup> 

<sup>a</sup>Fraunhofer IWM, MikroTribologie Centrum  $\mu$ TC, Freiburg, Germany; <sup>b</sup>Institute for Machine Elements and Systems Engineering, RWTH Aachen University, Aachen, Germany; <sup>c</sup>Freiburg Materials Research Center, University of Freiburg, Freiburg, Germany; <sup>d</sup>Institute of Physics, University of Freiburg, Freiburg, Germany

## ABSTRACT

Solid lubricants such as polytetrafluoroethylene (PTFE) are used to lubricate rolling-element bearings (REBs) when grease or oil cannot be applied. To compensate for PTFE's high wear, the rolling contacts can be relubricated by solid transfer films that form at the sliding contacts between the rolling elements and PTFE reservoirs in the cage pockets. Excessive PTFE relubrication causes a rapid depletion of the PTFE reservoirs, while insufficient PTFE relubrication leads to high friction and wear. Both situations can limit the REB's lifetime. In this study, we use a ball-on-disk tribometer enhanced with a PTFE relubricating pin as a model system for sliding and rolling contacts in an REB. Using the spacer layer imaging method (SLIM), we measure the film thickness distribution in the rolling point contact for different normal loads applied to the PTFE pin. This reveals spatially and temporally inhomogeneous films. Non-reactive, all-atom molecular dynamics (MD) simulations show that the PTFE lubricating film can be described as a Herschel-Bulkley fluid with a yield stress that is caused by perturbations of the perfectly layered molecular flow. By combining the MD-derived friction laws with the experimental film thickness distributions, we can quantitatively reproduce the measured macroscopic friction coefficients. The study shows that a tradeoff between friction reduction and low lubricant consumption can be obtained with a homogenous PTFE lubricant film with a thickness of only about 20 nm.

## ARTICLE HISTORY

Received 28 January 2025  
Accepted 6 May 2025

## KEYWORDS

PTFE; rolling-element bearings; solid lubrication film thickness; friction mechanisms; DFG SPP 2074

## Introduction

Polytetrafluoroethylene (PTFE) is probably the most prominent example of a polymeric solid lubricant and has been the subject of tribological investigations for well over half a century. (1,2) Because of its excellent low-friction properties, vacuum compatibility, chemical inertness, and applicability in a wide temperature range, it is well established in space tribology and many other applications such as seals and plain bearings as well as rolling-element bearings (REBs). (3,4)

PTFE's exceptional slipperiness is a result of its low cohesion in the shearing direction, (5) which makes the shear resistance within PTFE very low. For the same reason, PTFE transfer films on tribological surfaces can form even for low values of the surface-PTFE adhesion. (5) Origins of this behavior include:

- i. Shear-induced orientation of the PTFE molecules with the sliding direction. (6–9) Sliding along the chain direction of an oriented PTFE film results in substantially lower friction than sliding perpendicular to it. (10)

- ii. PTFE's molecular structure with very long, unbranched molecules without side groups that would disturb the intermolecular "flow." (5,11,12) Even small structural deviations such as the partial replacement of fluorine atoms along the carbon chains with larger chlorine atoms (PCTFE) or with CF<sub>3</sub> groups (Teflon-FEP) were reported to increase friction substantially. (9)
- iii. Very dense packing of fluorine-carbon dipoles along the molecular chain that leads to negligible electrostatic interactions between the molecules (despite the high polarity of the C-F bond). (13)
- iv. Very dense packing of fluorine atoms along the carbon chain leading to "sub-atomically smooth" molecules with a small potential energy corrugation associated to the intermolecular sliding. (8,14)
- v. Low polarizability of fluorine that contributes to rather low van der Waals interactions between the chains. (15)

Despite its excellent frictional properties, lubrication with PTFE has at least two major drawbacks. First, the high

**CONTACT** Thomas Reichenbach  [thomas.reichenbach@iwm.fraunhofer.de](mailto:thomas.reichenbach@iwm.fraunhofer.de); Florian König  [florian.koenig@imse.rwth-aachen.de](mailto:florian.koenig@imse.rwth-aachen.de)

\*Stephan von Goedel and Thomas Reichenbach have contributed equally.

Review led by T. Blanchet.

© 2025 The Author(s). Published with license by Taylor & Francis Group, LLC.

This is an Open Access article distributed under the terms of the Creative Commons Attribution License (<http://creativecommons.org/licenses/by/4.0/>), which permits unrestricted use, distribution, and reproduction in any medium, provided the original work is properly cited. The terms on which this article has been published allow the posting of the Accepted Manuscript in a repository by the author(s) or with their consent.

stability of fluorocarbons can lead to their accumulation in the environment. For this reason, potential upcoming restrictions and regulations (16) cause uncertainty and make further development and optimization of PTFE-lubricated machine elements questionable, even in closed systems. Second, PTFE is known for its high wear rate, (8) particularly at high contact pressures. A PTFE lubrication film can be removed easily from the contact zone under tribological load. (17) Once pushed to the sides of the contact zone, the solid lubricant does not flow back into the contact zone and therefore cannot contribute to the separation of the surfaces.

A possible, widely used solution to increase PTFE's wear resistance is to use it as composite material together with other materials with higher wear resistance such as polyetheretherketone (PEEK), (18,19) polyamide, (20) alumina, (21) and many others. (22–25) Another viable option, which we explore here, is to constantly resupply PTFE into the contact zone to compensate for the wear losses. In REBs, where the rolling elements are separated by a cage, this can be technically implemented by exploiting the double transfer mechanism (26): From the cage, which acts as a lubricant reservoir, the solid lubricant is gradually transferred to the rolling elements and is then further transported to the inner and outer races. Both excessive PTFE relubrication, causing a rapid depletion of the PTFE reservoirs in the cage, and insufficient PTFE relubrication, leading to high friction and wear, can limit the lifetime of such a bearing.

In this study, we investigate PTFE friction and double transfer mechanisms in rolling-point contacts with two goals in mind. The first one is the optimization of the PTFE lubrication in the context of the aforementioned compromise, that is, how much PTFE is required in the rolling contact for effective lubrication under the constraint of low PTFE lubricant consumption? The second, more general goal is to deepen the understanding of the PTFE friction and lubrication mechanisms, which can potentially help to find adequate fluorine-free alternatives.

In a previous study, we directly addressed PTFE lubrication in REBs experimentally and using atomistic simulations. (7) We used a ball-on-disk tribometer (mimicking the ball-race contact) enhanced with a PTFE pin, which was pressed against the disk (mimicking the resupply of the bearing from the cage that acts as a lubricant reservoir). We found that an increase in the PTFE supply enabled by increasing the normal load on the PTFE pin causes a decrease of friction in the rolling contact. The values of the central film thickness in the rolling contact, as measured by means of white-light interferometry, scatter strongly. However, in line with the accompanying MD simulations, the reduction in friction with increasing pin load could be linked to an increase in mean thickness values. Moreover, the simulations revealed that shear causes the PTFE chains to align with the shearing direction thus facilitating homogeneous flow within PTFE and decreasing shear resistance.

In the work presented here, we increase the resolution of the experiment by locally resolving the film thickness on the  $\mu\text{m}$ -scale using the spacer layer imaging method (SLIM) (27) instead of measuring only the central film thickness. In

the simulation part of the study, we build on our previously presented model (7) and systematically consider PTFE film thickness values comparable to those measured in the experiment. Additionally, we address the influence of the PTFE chain length. Combining the experimentally measured film thickness distribution with MD-derived friction laws allows us to go beyond the previously established qualitative correlation between friction reduction with increasing PTFE film thickness and to obtain a quantitative correlation.

## Methods

### Experimental setup

#### Tribometer

To measure the film thickness and coefficient of friction (COF) in a PTFE-lubricated rolling point contact, we reuse and adapt the setup presented in our previous publication, (7) which consists of a modified ball-on-disk tribometer (EHD2, PCS Instruments) as illustrated in Fig. 1. To enable film thickness measurements, we use an optically-transparent glass disk. This setup is typically used for research on the film formation of lubricating oils or greases in an elastohydrodynamic (EHD) rolling point contact. (28,29) For the double transfer mechanism, the tribometer is extended by an additional PTFE pin that is pressed on the disk and that transfers PTFE onto the disk, that is, it acts as a lubricant reservoir.

The diameters of the PTFE pin and steel ball are 4.3 mm and 19.05 mm, respectively. Both are running on the same disk radius. Roughness values of the disk and the ball, determined by using an atomic force microscope, (30) are given in Table 1 alongside the Young's moduli and Poisson ratios.

The amount of PTFE transferred from pin to disk is controlled by applying dead loads of various weights corresponding to forces on the pin  $F_{\text{pin}}$  between 0 and 100 N. Without dead load (i.e.,  $F_{\text{pin}} = 0$ ), the pin is still slightly pressed against the disk due to the dead weight of the apparatus with a force of about 0.1 N. The polished steel ball runs on the transfer film resulting in a ball running track within the sliding track. Using an electronically controlled system, a normal force  $F_{\text{ball}} = 20 \pm 2 \text{ N}$  is applied to the rolling contact for all experiments presented here. Using Hertzian contact theory and the elastic material properties given in Table 1, the pressure in the rolling contact is estimated to be about 526 MPa. We drive the ball and disk at velocities  $v_{\text{ball}} = 380 \text{ mm/s}$  and  $v_{\text{disk}} = 420 \text{ mm/s}$ , respectively, resulting in a slide-to-roll ratio (SRR) of 10% and a relative velocity of 40 mm/s between them. The COF is determined using the measured torque  $T_{\text{friction}}$  at the ball drive shaft. The measured friction is composed of the friction in the rolling contact and an additional offset caused by the friction components of the ball drive. To determine and compensate for this offset, we use two different approaches. In the first one, we follow Guegan et al. (31) and measure the torque in pure rolling (SRR = 0%) for  $F_{\text{ball}} = 20 \text{ N}$ . In the second approach, we measure the friction at positive and negative SRR values of equal magnitude for selected pin loads. For negative SRR the friction torque is negative, while

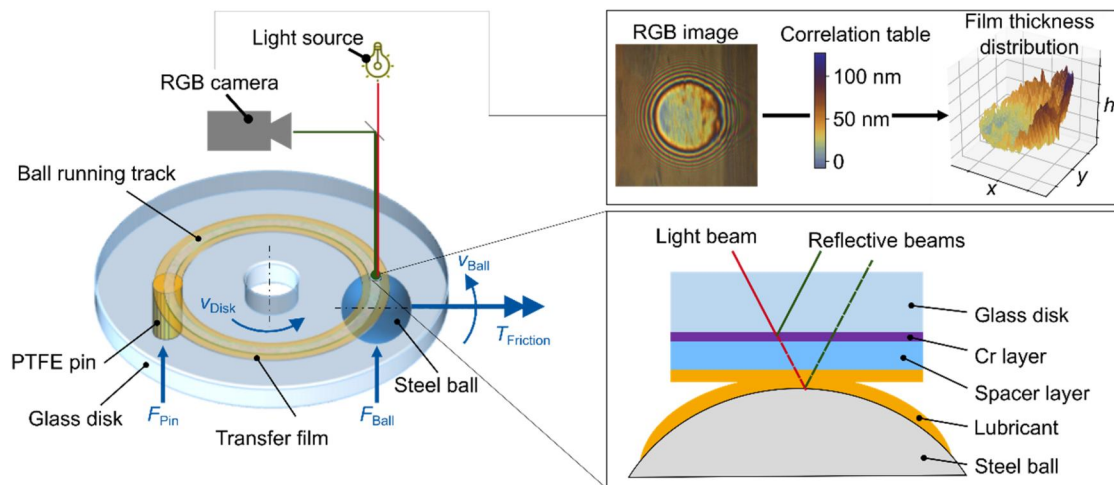


**Figure 1.** Schematic experimental setup consisting of a ball-on-disk tribometer with an additional PTFE pin that is pressed against the disk and acts as a lubricant reservoir. In the ball-disk contact, the friction and the film thickness distribution by means of the spacer layer imaging method (SLIM) are recorded.

**Table 1.** Material properties of the specimens.

Parameter	Glass disk	Steel ball
Young's modulus	75 GPa	207 GPa
Poisson ratio	0.22	0.29
$R_q$	0.8 nm	6.1 nm

for positive SRR it is positive, because the relative velocity between ball and disk changes sign. However, the direction of rotation of the ball drive shaft is the same for positive and negative SRR and the offset friction torque has the same sign for positive and negative SRR. As a result, the average of positive and negative torque values is equal to the offset value. The two approaches give offset values of 0.0198 and 0.0201, respectively. All COF values below are therefore corrected by an offset of 0.02. The experiment is performed at 40 °C. The temperature is measured and electronically controlled using a sensor in the immediate vicinity of the rolling contact.

The measurement protocol is as follows. Each measurement series covers all pin loads considered once (100 N, 80 N, 60 N, 40 N, 20 N, 0 N). For each series, we use a new steel ball and a new track, that is, a different radius on the glass disk. In order to run multiple measurement series on the same disk, this radius is varied between 36 and 42 mm in increments of 0.5 mm, while maintaining the same velocity and SRR. We obtain statistically the same results when repeating the experiment with different radii, indicating that the influence of a different number of ball rotations per disk rotation is within the experimental error bars. For each pin load, starting from 100 N in descending order, we initially clean both specimens using acetone. Then, an initial PTFE transfer layer is applied onto the surface of the glass disk by loading the PTFE pin with  $F_{Pin} = 20$  N against the glass disk (rotating with a speed of 400 mm/s) for 5 min, while the steel ball is not yet in contact with the disk. Afterward, the steel ball is positioned on the glass disk, such that it runs in the sliding track of the pin for 2 min to transfer PTFE from the disk onto the ball. After this run-in process is completed, we measure the friction in the rolling contact for  $F_{Pin}$  between 0 N and 100 N, (corresponding to

pressures in the pin-disk contact between 6.9 and 6,900 kPa) for 330 s. To assess the reproducibility of our results, we conduct the measurement series three times.

#### Film thickness measurement

The film thickness distribution in the ball-disk contact zone is measured in-situ using the SLIM. (27) In contrast to a post-mortem analysis of the worn samples, this approach allows for an unambiguous monitoring of the PTFE film in the contact under tribological load. From a source of white light, a light beam is directed through the glass disk into the rolling contact. At a semi-transparent chromium layer on the lower side of the glass disk the beam is split into a reference and a measurement beam. While the reference beam is reflected directly to the camera, the measurement beam passes through the chromium layer, a SiO<sub>2</sub> spacer layer and the PTFE film reaching the steel ball surface, where it is reflected. The measurement beam then re-transmits through the lubricant, the different layers and the glass disk to the camera. The different path lengths of the reference and measurement beam result in a phase difference and depending on the film thickness and the wavelength of the light beam, constructive and destructive fringes are created. Since white light is used, this yields a colored interferogram. We note that within this approach we assume that air gaps within the lubricant in the contact zone are negligible (i.e., if present, they are treated as if they had the refractive index of PTFE). We record the images of the interferogram using a red-green-blue (RGB) camera about every 3 s.

Each image has a resolution of  $1,024 \times 768$  pixels, with each pixel corresponding to a spatial extension of about  $0.8 \mu\text{m} \times 0.8 \mu\text{m}$  per pixel. We convert the RGB values of each pixel to a film thickness value using a correlation table. To create the correlation table, we perform two measurements with an FVA3 oil, (32) which matches the refractive index of PTFE with a deviation below 5%. First, the central film thickness of the EHD oil film is measured using the ultra-thin-film interferometry method (33) at various rolling speeds. This establishes the correlation between film

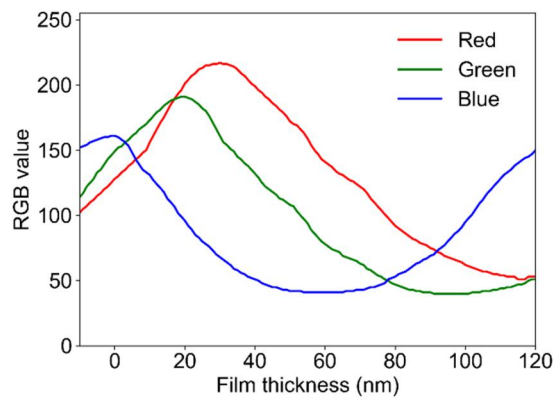


**Figure 2.** Correlation between spacer layer imaging method (SLIM)-derived red-green-blue (RGB) values and the central film thickness, as determined by ultra-thin-film interferometry, established with an FVA3 oil whose refractive index is within 5% of that of polytetrafluoroethylene (PTFE).

thickness and rolling speed. In the second measurement, images of the EHD oil film are captured under identical contact conditions and various rolling speeds using the SLIM. The RGB values in the central contact area are then determined and correlated with the rolling speed. By comparing the results of both measurements, we establish a correlation between film thickness and RGB value, as shown in Fig. 2.

To convert an RGB image into a 3D film thickness map, the film thickness for each pixel is determined from this correlation by identifying the RGB values ( $r_c, g_c, b_c$ ) of the calibration table that best match the pixel's RGB values ( $r, g, b$ ). As an error metric, we use  $d = \frac{1}{255} \sqrt{(r - r_c)^2 + (g - g_c)^2 + (b - b_c)^2}$ . To avoid incorrect detection of film thickness values, which can occur due to intensity shifts and fringe order ambiguities (see MacLaren et al. (34) for a discussion), we limit the correlation table to film values between  $-10$  nm and  $120$  nm. If the minimal deviation  $d$  from any of the RGB values in the calibration table is greater than  $0.002$ , the film thickness is considered to be greater than  $120$  nm.

### Atomistic simulations

To study the lubrication mechanisms of PTFE in the ball-disk contact and the relationship between film thickness and shear stress, we use classical MD sliding simulations of PTFE-lubricated hematite contacts. The atomistic model builds upon our earlier work (7) and is schematically illustrated in Fig. 3.

Hematite is chosen as a representative model of oxidized steel surfaces. (35) For simplicity, we use this model for both surfaces. As discussed in the following section, PTFE sticks to the surfaces and the entire shear deformation is accommodated within the PTFE phase. For this reason, we do not expect this simplification of the experimental material to be critical and expect comparable results with other surface models as long as there is no slip at the PTFE/surface interfaces. (36) In fact, the atomically-flat iron oxide surface model used here is more prone to slip than an

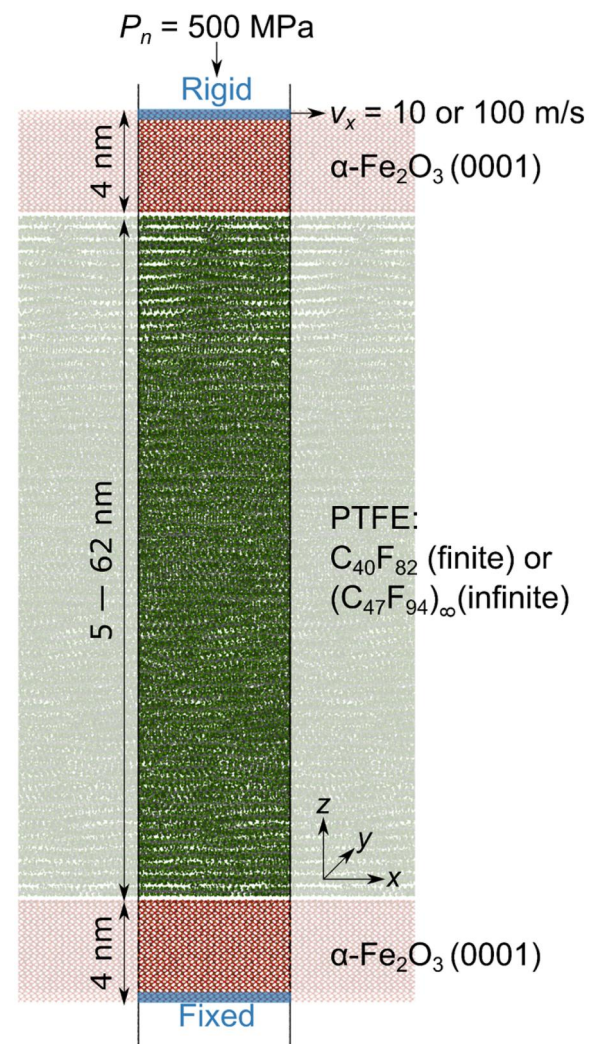


**Figure 3.** Molecular dynamics (MD) simulation setup consisting of a  $\alpha$ -Fe<sub>2</sub>O<sub>3</sub>(0001)/ $\alpha$ -Fe<sub>2</sub>O<sub>3</sub>(0001) sliding interface that is lubricated with different amounts of polytetrafluoroethylene (PTFE). Periodic boundary conditions are applied along the  $x$  and  $y$  directions. PTFE is either modeled using C<sub>40</sub>F<sub>82</sub> oligomers or infinite chains resulting from the periodic repetition of C<sub>47</sub>F<sub>94</sub> units. Oxygen (O), iron (Fe), carbon (C), and fluorine (F) atoms are visualized as red, brown, gray, and green spheres, respectively.

intrinsically rough amorphous silica surface, which would be the natural choice for representing the glass disk in a more sophisticated interface model.

We pair two Fe-terminated  $\alpha$ -Fe<sub>2</sub>O<sub>3</sub> (0001) slabs, each of which is composed of 12,960 atoms and has spatial extensions of  $6.086 \times 5.270 \times 4.3$  nm<sup>3</sup>. Periodic boundary conditions are used in the interface plane. To apply a shear deformation to the system, we keep the atomic positions of a 4 Å-thick region of the lower slab fixed, while we drive a 4 Å-thick, rigid region of the upper slab at constant velocity (see Fig. 3). We note that the mixed sliding and rolling of the experiments is approximated as pure sliding under normal pressure in this atomic-scale computational setup.

The typical molecular weight of PTFE is on the order of  $10^6$ – $10^8$  g/mol (37) corresponding to at least 20,000 repetitive CF<sub>2</sub> units. Since this length scale is beyond what is feasible in our all-atom MD simulations, we instead consider two limiting cases to model PTFE. The first case considers PTFE molecules with a finite length, that is, C<sub>40</sub>F<sub>82</sub>. Note

that even when fully stretched and aligned with the sliding direction, the end-to-end distance of these molecules ( $\sim 5.1$  nm) is shorter than the simulation cell dimension along the sliding direction (6.086 nm). The second limiting case consists of  $C_{47}F_{94}$  units that have approximately the same length as the simulation cell along  $x$  direction so that their periodic repetition results in infinitely long chains that are aligned with the sliding direction, which we refer to as  $(C_{47}F_{94})_{\infty}$  in the following. In our previous study, (7) we showed that at the nanoscale shear causes an alignment of the PTFE molecules with the sliding direction, resulting in a pseudo-crystalline arrangement that is reminiscent of the hexagonal phase II of PTFE. (38) For the present study, we already pre-align all PTFE molecules with the sliding direction on a hexagonal lattice with 9 molecules per PTFE layer. Additionally, each molecule is initially randomly displaced along the direction of sliding. In contrast to the molecular length, the typical PTFE film thicknesses in the ball-disk contact measured in the experiment can be matched directly. We consider for both PTFE models the following numbers of molecules: 99, 207, 405, 603, 801, 1,008, 1,206; corresponding to film thicknesses between about 5 and 61 nm and a total number of atoms between 37,998 and 195,966.

The experimental relative velocity between ball and disk is 40 mm/s. Using the same value for the sliding velocity in the simulation would not allow us to sample the sliding motion in a representative way. For this reason, we consider two different, much higher velocities, 10 m/s and 100 m/s, to assess the influence of the sliding velocity on the shear stress and enable its extrapolation to the experimental velocities. The resulting high shear rates would cause the temperature in the PTFE phase to increase substantially when applying thermostats just to parts of the hematite slab that are far from the sliding interface, as in our previous work. (7) While our previous simulations only addressed film thicknesses below 25 nm and this issue did not arise, here we deal with lubricant film thickness values up to 61 nm. Therefore, we apply a Langevin thermostat with a target temperature of 300 K and a damping constant of 1 ps to all atoms except for the rigid and fixed ones. The thermostat acts only along the direction perpendicular to the sliding direction and the normal load direction to reduce the effect of the thermostat's dissipation on the shear stress. We apply a normal pressure of 500 MPa, which approximately corresponds to the Hertzian contact pressure in the ball-disk contact (see the Experimental Setup section).

For the interatomic interactions we reuse our previous model, (7) where PTFE is described using the all-atom force field for perfluoroalkanes by Watkins and Jorgensen, (39)  $\alpha$ - $Fe_2O_3$  (0001) is described by a harmonic spring model, and the  $\alpha$ - $Fe_2O_3$ -PTFE interaction is represented by an effective Lennard-Jones potential that was fitted to density-functional theory reference calculations.

All simulations follow the same protocol: We first relax the initial structure while keeping the atomic positions in the constrained regions fixed, then equilibrate the system under a constant pressure and temperature. Afterwards, we

start sliding by applying a constant velocity of 10 or 100 m/s to the upper rigid layer while keeping the system under a normal pressure of 500 MPa with the pressure-coupling algorithm of Pastewka et al. (40) As soon as the system's height has stabilized at a constant value, we switch to constant-height simulations to reduce the noise in the velocity profiles. The average pressures during the constant-height simulations deviate at most 25 MPa from the target value of 500 MPa. All reported quantities are averaged over these steady-state simulations, which have a duration of 4 ns for the 10 m/s case, and a duration of 2 ns for the 100 m/s case. To roughly estimate the spread of the shear stresses, we compute the mean and the standard deviation from measurements in three distinct intervals: (0, 500) ps, (750, 1250) ps, and (1500, 2000) ps for the 100 m/s case and (0, 1000) ps, (1500, 2500) ps, and (3000, 4000) ps for the 10 m/s case. Shear stresses are calculated as the sum of the forces on the upper rigid layer along the sliding direction normalized by the cell area. PTFE film thicknesses are measured as the difference between the lowest coordinate of the upper  $\alpha$ - $Fe_2O_3$  slab and the topmost coordinate of the lower  $\alpha$ - $Fe_2O_3$  slab after the system has reached the steady-state height. Time integration is performed with a timestep of 0.5 fs.

## Results and discussion

### Friction, film thickness, and coverage measurements

Figure 4 shows the COF in the ball-disk contact as a function of time for six different pin loads  $F_{pin}$  ranging from 0 N to 100 N. For each load, the COF remains stable over the measured period. In agreement with our earlier results, (7) there is a trend of a decreasing COF with increasing pin load. The largest impact of the pin load can be observed when going from  $F_{pin} = 0$  to  $F_{pin} = 20$  N, where the averaged COF reduces from 0.065 to about 0.044. Further increases in pin load result in less pronounced friction reductions and eventually to a saturation at around 0.035 for the highest pin loads of 80 N and 100 N. The results indicate that the double transfer mechanism in our setup works and PTFE is transferred from the pin to the ball-disk contact.

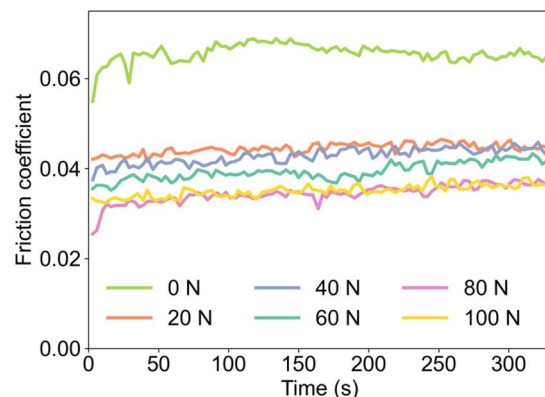
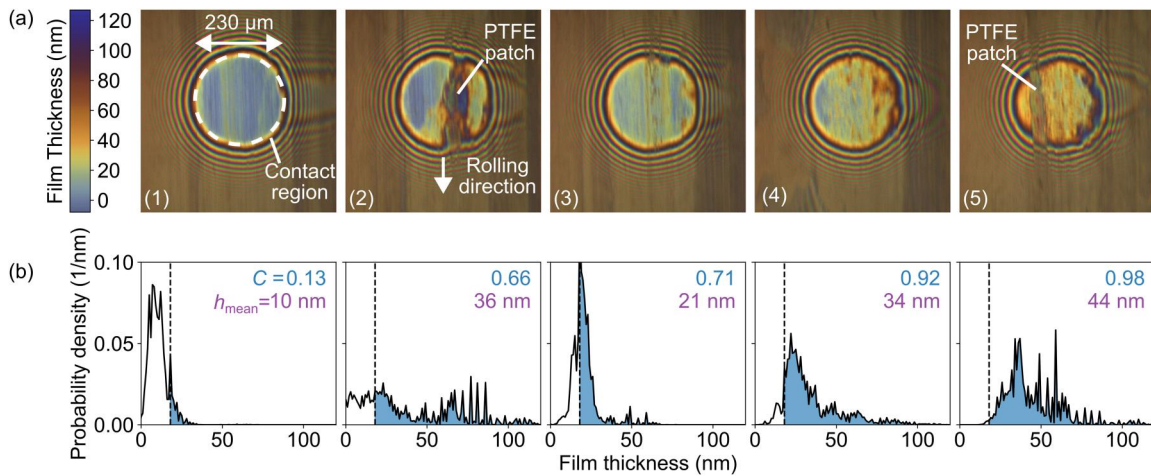


Figure 4. Coefficient of friction (COF) in the ball-disk contact as a function of time for pin loads  $F_{pin}$  between 0 and 100 N.



**Figure 5.** Exemplary spacer layer imaging method (SLIM) images of the rolling contact (a) and the corresponding film thickness distributions in the contact region (b). In panel b, the fraction  $C$  of the contact region in which the film thickness is at least 18 nm is indicated in blue in the upper right corner of each subplot. The mean film thickness in the contact region  $h_{\text{mean}}$  (as defined in the text) is written in violet.

A more direct analysis of the lubrication process is provided by the SLIM images of the ball-disk contact. In contrast to the low scattering in the time evolution of the COF, these images show a large variation within the same experiment: Film thicknesses and distributions are spatially and temporally inhomogeneous. Prior to proceeding with a more rigorous statistical data evaluation, we first discuss some typical scenarios with different film thicknesses and distributions to introduce our analysis approach and the corresponding relevant quantities. Figure 5a shows five exemplary images recorded for  $F_{\text{pin}} = 20$  N, but because of the large variations they could have been taken at any of the pin loads considered. Initially, using an unlubricated contact, we identify the contact zone for the ball load  $F_{\text{Ball}} = 20$  N by detecting the onset of the interference patterns that indicate the increase of the air gap between ball and disk surfaces (each repetition of color indicates the passing of one interference order). For the analysis of the lubricated contacts, we consider the same contact zone. Within the contact zone, film thickness values up to 120 nm can be reliably determined from the RGB values for each pixel using a correlation table (see color scale in Figs. 2 and 5a). While exact film thickness values above 120 nm cannot be quantified, we can determine if the film thickness of a pixel is above this value.

For a quantitative analysis of the film thickness distributions, we convert the RGB values into film thicknesses and determine their frequency of occurrence in the contact region. Figure 5b shows the distribution functions  $f(h)$  of the film thickness  $h$  in the contact region for each of the five example images. The binning of the distributions is done in steps of 1 nm and the distributions are normalized such that  $\int_0^{\infty} f(h) dh = 1$ . To compare different distributions, we compute the integral of each distribution function starting from a threshold thickness value of 18 nm:  $C = \int_{18}^{\infty} f(h) dh$ .  $C$  corresponds to the fraction of the contact region that is separated by at least 18 nm (indicated in blue in the upper right corner of the diagrams) and is referred to as (lubricant) coverage throughout this article. This

threshold value is chosen for two reasons. First, for the given combined roughness of the glass and ball surfaces  $\sigma = \sqrt{R_{q,\text{disk}}^2 + R_{q,\text{ball}}^2} = 6.15$  nm (see Table 1), a central film thickness of about 18 nm roughly indicates the onset of the full film lubrication regime. At this point the dimensionless  $\lambda$  parameter, which is defined as the ratio between the central film thickness and  $\sigma$ , becomes larger than three. (41) Second, as shown in the following section using the MD simulations, starting at about 18 nm the shear stresses only decrease marginally with increasing film thickness. For each distribution, we also calculate the mean film thickness  $h_{\text{mean}} = \int_0^{\infty} f(h) h dh$ . In this calculation, we treat film thicknesses larger than 120 nm as having a thickness of 120 nm as our method becomes unreliable for thicker films. As we will see in the following section, further increasing the film thickness above 120 nm does not significantly reduce friction anymore.

In image 1 of Fig. 5a, a rather uniform but very thin film can be observed with a distribution peak around  $h_{\text{mean}} = 10$  nm. 87% of the contact region has a film thickness below 18 nm, that is, the coverage  $C$  is 0.13. Image 2 shows a very inhomogeneous distribution with an overall coverage  $C$  of 0.66 and  $h_{\text{mean}} = 36$  nm. The left part of the contact has only a minimal amount of PTFE in the contact (film thickness mostly below 18 nm), while a thick PTFE patch can be observed in the right part. The exact thickness of such big patches cannot be determined using the SLIM (and therefore it does not enter the calculation of  $h_{\text{mean}}$ ). However, using the method described in Ye et al., (42) we estimate the thickness of such patches to be several hundred nanometers by counting the repeated occurrence of the interference colors (i.e., the interference order). This is reminiscent of the observations in Lu et al., (17) where PTFE transfer films have been reported to have two forms: PTFE patches with thickness on the scale of microns that can act as local PTFE reservoirs, and thin films of a few nanometers that are thought to be responsible for low friction. Image 3 shows a rather uniform distribution with the main peak shifted toward higher thicknesses such that  $C = 0.71$ , even though

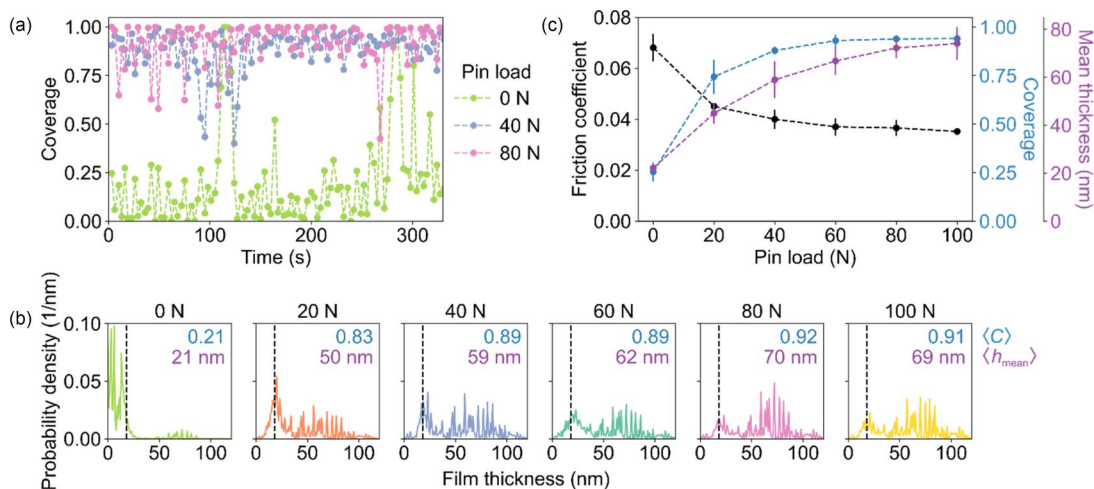


**Figure 6.** (a) Coverage  $C$ , as a function of time for three different pin loads. (b) Averaged film thickness distributions  $\langle f \rangle$  for different pin loads. Each distribution is averaged over 100 images recorded within a period of 330 s. The vertical dashed lines indicate a film thickness of 18 nm and the blue numbers in the upper right corners are the average coverage  $\langle C \rangle$ . The violet numbers show the mean film thickness  $\langle h_{\text{mean}} \rangle$ . (c) Average COF, average coverage and average mean film thickness as a function of the pin load. Each data point represents three independent measurements. For each measurement we determine the average film thickness distribution and, from that distribution, the average coverage and average film thickness. Error bars show the standard deviation of the three measurements.

the average film thickness  $h_{\text{mean}} = 21$  nm is significantly smaller than the one in image 2. In image 4 almost the full contact is rather homogeneously covered in PTFE with a thickness larger than 18 nm ( $C = 0.92$ ) and a  $h_{\text{mean}}$  comparable to the one in image 2. Finally, in image 5 the contact is excessively lubricated with PTFE including large patches ( $C = 0.98$ ,  $h_{\text{mean}} = 44$  nm).

To show how the film distributions scatter during the experiment for the different pin loads, we determine the film thickness distribution and the corresponding lubricant coverage  $C$  as a function of time, as illustrated for three pin loads (0 N, 40 N, 80 N) in Fig. 6a. In all three cases there is significant scatter with variations that are larger than 0.4. The scatter decreases with increasing pin load, while the mean  $C$  values increase. The increase in coverage is also evident by considering the film thickness distributions averaged over time  $\langle f \rangle$  (330 s, 100 RGB images) shown in Fig. 6b (in the following, we use angle brackets to indicate time averages). While for  $F_{\text{pin}} = 0$  N  $\langle f \rangle$  is narrow and centered on film thicknesses below 18 nm, the distribution moves toward higher thicknesses and becomes broader with increasing pin load. This is also reflected in the averaged coverages  $\langle C \rangle = \int_{18}^{\infty} \langle f(h) \rangle dh$  that initially increase very rapidly and eventually converge at around 0.9 for pin loads starting from about 40 N. The mean film thickness  $\langle h_{\text{mean}} \rangle = \int_0^{\infty} \langle f(h) \rangle h dh$  follows a similar trend but only converges for the highest pin loads of 80 N and 100 N.

Figure 6c shows the average COF, average coverage  $\langle C \rangle$  and the mean film thickness  $\langle h_{\text{mean}} \rangle$  as a function of the pin load, where we average the data over three independent runs of the experiments. This data clearly reveals that the coverage  $\langle C \rangle$  and the mean film thickness  $\langle h_{\text{mean}} \rangle$  can be controlled by the pin load. Both quantities are closely connected, even though one does not necessarily imply the other, particularly without time averaging as we have previously discussed (c.f., the  $C$  and  $h_{\text{mean}}$  values in Fig. 5). Thicker films (on average) favor higher coverages, but there can be uniform films with same  $\langle C \rangle$  and different  $\langle h_{\text{mean}} \rangle$ .

All three curves converge to a constant value for large pin loads, although the convergence of the coverage and the COF is slightly faster than the convergence of the film thickness. This suggests that, in order to reduce friction, it is more critical to minimize the part of the contact that is only poorly lubricated than to lubricate with thicker films. Indeed, the COF does not change significantly for average film thicknesses above 60 nm.

According to the literature, (43) the wear rates of the pin can be expected to increase at a rate that is faster than linear with increasing pin load. Combined with the fact that coverage and mean film thickness converge, this shows that the PTFE relubrication of the ball-disk contact with the double transfer mechanism becomes less and less effective with increasing pin load: Even though more and more lubricant is released onto the disk, the amount of PTFE material in the ball-disk contact saturates.

### Simulation results

To investigate lubrication mechanisms that are inaccessible to our experimental analysis, we use non-reactive MD simulations of PTFE-lubricated contacts. The main goal is to study how friction locally depends on the PTFE film thickness for thicknesses up to 60 nm, that is, on the lower end of the experimental values, in order to find friction laws that describe the friction-thickness relationship. In a subsequent step, we combine these laws, extrapolated to the experimental conditions, with the experimental film thickness distributions to rationalize the macroscopic coefficients of friction.

We reuse our previous computational setup and consider PTFE-lubricated hematite contacts. (7) To reduce the computational time required to align the PTFE chains with the shearing direction and reach a steady-state, (7) we directly pre align the chains with the sliding direction (details in Methods). Figure 7a shows the averaged shear stress of PTFE-lubricated hematite contacts under a normal pressure

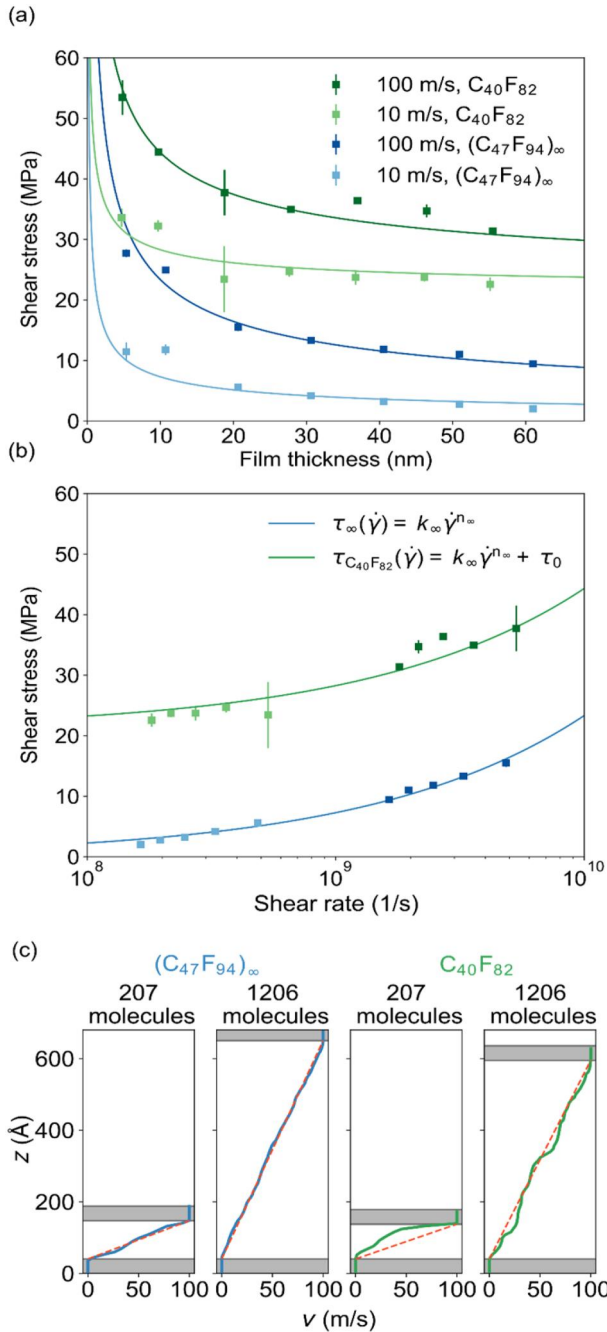


**Figure 7.** Shear stress as a function of the polytetrafluoroethylene (PTFE) film thickness (a) and of the average shear rate in PTFE (b) for an applied sliding velocity of 10 or 100 m/s and PTFE modeled either as finite  $C_{40}F_{82}$  molecules or as infinite  $(C_{47}F_{94})_{\infty}$  chains. Solid lines show fits to the data in panel b, where the PTFE model with infinite chains is described as a power-law fluid and the case of the finite oligomers as a power-law fluid with the same parameters plus an additional offset (i.e., a Herschel-Bulkley fluid). Error bars indicate the standard deviation of three measurements in distinct time intervals (Methods). (c) Velocity profiles of PTFE-lubricated  $\alpha$ - $Fe_2O_3$  contacts sheared at 100 m/s, where PTFE is modeled as infinite  $(C_{47}F_{94})_{\infty}$  chains (blue curves) or as finite  $C_{40}F_{82}$  molecules (green curves). Each column refers to a simulation with a number of molecules specified in the respective title. The grey-shaded area represents the  $\alpha$ - $Fe_2O_3$  slabs. The red dashed lines show idealized linear profiles of a homogeneous PTFE flow. Their slopes are calculated by dividing the applied velocity by the PTFE film thickness. Profiles are averaged over 2 ns and collected in bins with a height of 8 Å.

of 500 MPa for four cases: PTFE modeled as finite  $C_{40}F_{82}$  molecules or as  $(C_{47}F_{94})_{\infty}$  (chains with infinite length), both with sliding velocities of 100 m/s and 10 m/s.

The data show clear trends within the considered parameter space: (i) the shear stress decreases with increasing film thickness and the largest variations are found for thicknesses below  $\sim 18$  nm (justifying the choice of a threshold of 18 nm for the coverage  $C$ ); (ii) the finite size of the molecules significantly increases the shear stresses compared to the infinite-chain case; (iii) a higher sliding velocity (i.e., a higher shear rate) increases friction; (iv) the finite size of the molecules increases the scattering of the data.

To find a friction law, we aim for the simplest model that fits the data starting from the case of the infinite chains. For this purpose, we plot the shear stress as a function of the shear rate (Fig. 7b) for the cases with a film thickness above 15 nm to mitigate the influence of the surfaces. The shear rate is approximated as the average shear rate  $\dot{\gamma} = v/h$ , where  $h$  is the PTFE film thickness and  $v$  the applied velocity. This is justified by the fact that the shear deformation is not localized at an atomically sharp interface, as one might expect for solid contacts, but is instead distributed over the entire PTFE phase with an approximately linear velocity profile (Fig. 7c), which closely follows this homogeneous shear flow approximation (red lines). Wall slip turns out to be negligible in these systems, even without chemical bonds between PTFE and the surface. While the data points for the infinite chains in Fig. 7b cannot be described by a Newtonian fluid (i.e., a one-parameter model with a constant viscosity), we find that a two-parameter power law

$$\tau_{\infty}(\dot{\gamma}) = k_{\infty} \dot{\gamma}^{n_{\infty}} \quad [1]$$

fits the data reasonably well, where  $k_{\infty}$  is the consistency and the exponent  $n_{\infty}$  accounts for the observed shear thinning. The fit yields  $k_{\infty} = 207 \pm 114 \text{ Pa} \cdot s^{n_{\infty}}$  and  $n_{\infty} = 0.51 \pm 0.03$ .

To describe the case of the finite chains, we note that with increasing film thickness, the shear stresses tend to converge toward a finite value larger than 0 (Fig. 7a). This is indicative of a yield stress that needs to be overcome to induce flow in the solid lubricant. Also in this case, we plot the shear stress as a function of the average shear rate in Fig. 7b for film thicknesses larger than 15 nm. While the velocity profiles are still roughly linear on average, as exemplarily shown in Fig. 7c, there are clear kinks and steps in the profiles that indicate that the shear flow is not entirely homogeneous and temporary shear localization can occur.

Remarkably, the data points of the finite chains are approximately parallel to the data points of the infinite chains (Fig. 7b). This suggests that the shear flow behavior is similar in both cases once the yield stress for the finite chains is overcome. In this spirit, we fit the data points by starting from  $\tau_{\infty}(\dot{\gamma})$  with fixed  $k_{\infty}$  and  $n_{\infty}$  and include a yield stress  $\tau_0$

$$\tau_{C_{40}F_{82}}(\dot{\gamma}) = \tau_{\infty}(\dot{\gamma}) + \tau_0 = k_{\infty} \dot{\gamma}^{n_{\infty}} + \tau_0. \quad [2]$$

This gives  $\tau_0 = 21.0 \pm 0.6$  MPa.

A natural explanation for  $\tau_0$  are the defects created by the finite length of the molecules that disturb the homogeneous shear flow within the pseudo-crystalline PTFE phase. To support this point, we analyze if and how the PTFE molecules extend over several PTFE layers. We calculate the

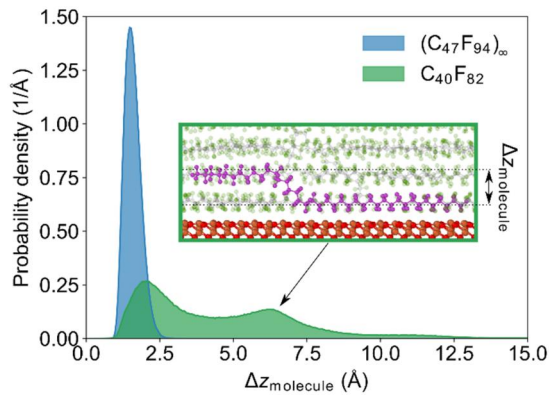


**Figure 8.** Probability density distribution of the spatial extension of the polytetrafluoroethylene (PTFE) molecules along the  $z$  direction for infinite  $(C_{47}F_{94})_{\infty}$  chains and for finite  $C_{40}F_{82}$  molecules.  $\Delta z_{\text{molecule}}$  is defined as the difference between the largest and smallest  $z$  coordinates of all carbon atoms in each molecule. Both distributions are averaged over all PTFE molecules and all snapshots of the 100 m/s sliding simulations with 1,206 PTFE molecules. The inset shows a  $C_{40}F_{82}$  molecule, highlighted in purple, that extends over two PTFE layers.

spatial extension of the molecules along the direction normal to the PTFE layers ( $z$  in Fig. 3) and use the difference between the largest and smallest position of the carbon atoms within each molecule as a measure ( $\Delta z_{\text{molecule}}$ ). Figure 8 exemplarily shows the distributions of  $\Delta z_{\text{molecule}}$  for the 100 m/s cases, where the contact is lubricated with 1,206 molecules. In the case of the infinite chains, there is only one large peak corresponding to PTFE molecules that are part of a single PTFE layer. For the finite chains, the distribution is smeared out significantly and a second peak at around 6.2 Å and a faint shoulder at  $\sim 10$ –11 Å emerge. These correspond to PTFE molecules that extend over 2 or even 3 PTFE layers as exemplarily illustrated in the inset of Fig. 8.

### Combining friction laws with experimental film thickness distributions

The friction forces measured in the experiment are the sum of the local shear forces, which vary with the local film thickness. In the following, we combine the friction laws with the averaged film thickness distributions of the experiment (as exemplarily illustrated in Fig. 6b) to make a prediction about the macroscopic COF and compare it to the measured values. The established friction laws allow for an extrapolation to the experimental conditions with relative velocities of 40 mm/s between ball and disk. We note that the experimental system is glass/PTFE/steel while we established the friction laws for hematite/PTFE/hematite contacts. Nonetheless, our estimates should be reasonable as long as the shear deformation is only localized within the PTFE phase and wall slip is negligible (as evident in the MD simulations from Fig. 7c). Moreover, in our previous publication with the same experimental setup, we compared a steel disk to a glass disk with similar surface roughness and found comparable COF—even for a PTFE pin load  $F_{\text{pin}} = 0$ . (7)

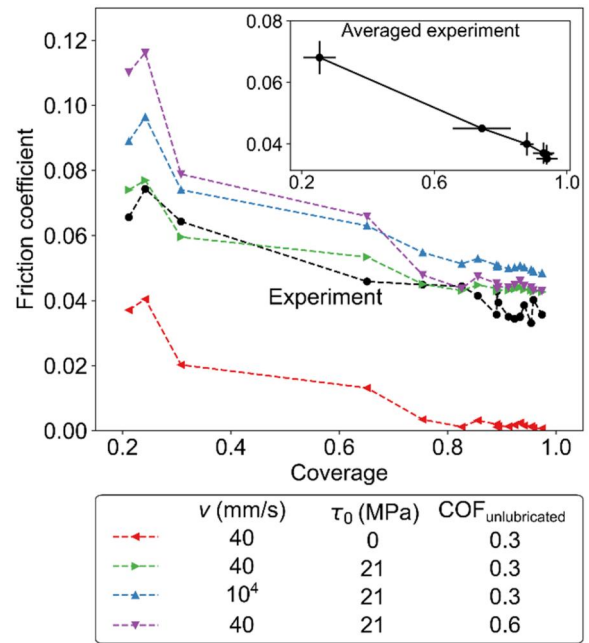


**Figure 9.** Coefficient of friction (COF) as a function of the average film coverage ( $C$ ). The black line shows the experimental results obtained for a relative sliding velocity of 40 mm/s between disk and ball. Each point corresponds to the average of one run of the experiment for a specific pin load. The prediction of our model that combines the molecular dynamics (MD) friction laws with the experimentally measured average film thickness distributions is shown for different combinations of the velocity  $v$ , the offset  $\tau_0$  and the friction coefficient for the insufficiently lubricated regions of the contact  $\text{COF}_{\text{unlubricated}}$ . In the inset the experimental values with the same pin load are averaged with the error bars showing the standard deviation (i.e., the data from Fig. 6c).

To predict a macroscopic shear stress  $\langle \tau \rangle$  from the averaged film thickness distributions  $\langle f(h) \rangle$  we use

$$\langle \tau \rangle(v, \tau_0) = \int_0^{\infty} \tau(h, v, \tau_0) \langle f(h) \rangle dh \quad [3]$$

with

$$\tau(h, v, \tau_0) = k_{\infty} \left( \frac{v}{h} \right)^{n_{\infty}} + \tau_0. \quad [4]$$

For the consistency and the exponent parameters, we use the values determined above by fitting the results of the MD simulations ( $k_{\infty} = 207 \text{ Pa} \cdot \text{s}^{n_{\infty}}$ ,  $n_{\infty} = 0.51$ ). To convert  $\langle \tau \rangle(v, \tau_0)$  to a COF, we simply normalize it by  $P_n = 500 \text{ MPa}$  (the normal pressure at which the friction laws were parameterized and which is close to the Hertzian pressure of 526 MPa in the experiment). To evaluate Eq. [3], a shear stress for  $h = 0$  is required. This is the shear stress of the solid–solid contact, which is a parameter of the model called  $\text{COF}_{\text{unlubricated}}$  in the following. To convert  $\text{COF}_{\text{unlubricated}}$  to  $\tau(h = 0)$ , we multiply it by the normal pressure 500 MPa. Moreover, because of the unreliability of the SLIM for thicknesses above 120 nm, we treat each film thickness above 120 nm as if the film thickness were 120 nm. This is a reasonable assumption because for such large values of the film thickness the shear stresses are insensitive to the thickness (Fig. 7), in particular for slow relative velocities as the one in the experiment.

Figure 9 shows the experimental coefficient of friction as a function of the coverage, evaluated from the averaged film thickness distribution function (black lines). By averaging the data over three independent runs for each pin load, we observe an almost perfect linear correlation (shown in the inset). However, the curve becomes more erratic if the individual runs are plotted independently (main graph), which reflects the fact that the PTFE film can be inhomogeneous as for example observed in image 2 of Fig. 5a. We can evaluate Eq. [3] for each of the data points in the main graph and their corresponding averaged film thickness distribution function. Using the experimental velocity  $v = 40$  mm/s,  $\tau_0 = 0$ , that is, assuming that the infinitely long PTFE chains are representative of the experimental material, and a velocity-independent coefficient of friction  $\text{COF}_{\text{unlubricated}} = 0.3$ , which has been reported for steel-glass contacts in vacuum, (44) we obtain the red curve in Fig. 9. Remarkably, the curve shows the features of the experimental curve and also the friction differences between the individual points. However, all COF values are shifted downwards by  $\sim 0.03$ – $0.04$ , which probably is the result of the highly idealized setup used to generate the friction laws with no perturbations of the intermolecular flow.

If we instead use the  $\tau_0$  parameter of the finite chains (21 MPa, corresponding to a COF shift of 21 MPa/500 MPa = 0.042) the resulting curve shown in green lies remarkably close to the experimental curve. Given the simplicity of our model this agreement should not be over-interpreted. While we might benefit from error cancelation, this still suggests that our model captures the aspects of the system that are relevant to friction reasonably well. The close agreement for a parameter  $\tau_0$  obtained for the very short chains can have different origins. In the simulations,  $\tau_0$  is the result of the finite chains disturbing the flow of the molecules. In the experiments, where the chains are much longer, the flow is additionally disturbed by the roughness of the surfaces resulting in an “effective”  $\tau_0$  of the same order of magnitude. Additionally, possible tribochemical reactions—which are not considered in our simulations—could cause structural changes within PTFE (11) such as cross-linking or chain shortening. This should also contribute to the  $\tau_0$  parameter. In this sense  $\tau_0$  could be interpreted as a measure of the “imperfection of the system”. Alternatively, the yield stress required to induce flow in PTFE could be (almost) independent of the chain length and might rather depend on the density of defects like the one shown in Fig. 8. While longer chains result in less defects, they can probably easily extend over more than just two or three PTFE layers and the distributions of Fig. 8 would be broader.

To show how sensitive the agreement is with respect to the other two parameters  $\text{COF}_{\text{unlubricated}}$  and the velocity  $v$ , we also show two additional curves, one in which we doubled  $\text{COF}_{\text{unlubricated}}$  to 0.6 (violet), and one in which we use the velocity of the simulations  $v = 10$  m/s (blue). Increasing the velocity by a factor of 250 shifts the curve to slightly higher COF values by about 0.01 to 0.02. Unsurprisingly, increasing  $\text{COF}_{\text{unlubricated}}$  by a factor

of 2 has a large influence for small coverages, while the curve remains approximately the same for coverages above 0.75.

## Conclusions

In this work, we explored the PTFE film formation and the frictional behavior in a rolling point contact between a steel ball and a glass disk lubricated with the double transfer mechanism. The study demonstrates that for the investigated surface roughness values an effective PTFE lubrication can be achieved with a homogeneous film of only about 20 nm in thickness. While thick patches were reported to act as local lubricant reservoirs, (17) they should be avoided to reduce consumption of lubricant in cases where PTFE is available otherwise (e.g., via the double transfer mechanism). Conversely, regions with thinner films can increase friction substantially. The PTFE transfer film is typically spatially and temporarily inhomogeneous and a measurement of the central film thickness is only suitable if averaged over a sufficient number of images. (7) To use PTFE lubrication effectively, future studies should address how a homogenization of the PTFE film thickness distribution can be achieved without increasing the film thickness above 20 nm. Moreover, understanding how the PTFE transport and the film thickness required for an effective lubrication in the rolling contact are affected by the surface roughness of the disk and ball would be an important step toward improving double-transfer-lubricated engineering components.

Our MD simulations revealed that PTFE can be described as a Herschel-Bulkley fluid and a yield stress must be overcome to induce flow in PTFE for finite chains as opposed to infinite chains. Further research should address the relationship between the yield stress and the chain length. If these relationships are reliably known, one could potentially even draw conclusions on the film thickness from the measured friction. Another natural follow-up to reduce length and time scale gaps between the experiment and the simulations would be to coarse-grain the all-atom simulations as recently performed by, for instance, in Xu et al. (6) and Brownell and Nair. (45) Ultimately, to help optimize the lifetime of double-transfer-lubricated systems, our PTFE friction laws should be combined with a wear model. The latter should quantitatively connect the lubricant consumption (i.e., PTFE wear in the pin-disk contact) with the film thickness and distribution in the ball-disk contact. While wear laws for PTFE sliding contacts exist in the literature, (43) further developments are necessary to model the transport of PTFE into the ball-disk contact and its squeeze-out.

In general, predicting friction and wear in rolling point contacts relubricated with the double-transfer mechanism based on the interplay between lubricant consumption, transfer film formation, film thickness and film distribution would be extremely helpful to rationally design double-transfer REBs and in particular their cages. The underlying fundamental mechanisms can be understood using the presented combination of SLIM and MD simulations. Future

studies should extend our findings to industrially relevant PTFE compounds and address how to achieve optimal lubrication in an actual REB, i.e., a sufficient solid lubricant supply for a low-friction operation on the one hand, and low compound wear to allow double transfer relubrication for extended periods on the other hand.

## Acknowledgements

T. Reichenbach thanks Hannes Holey for helpful discussions. T. Reichenbach, S. Peeters, G. Moras, and M. Moseler gratefully acknowledge the Gauss Centre for Supercomputing e.V. for providing computing time through the John von Neumann Institute for Computing (NIC) on the GCS Supercomputer JUWELS (46) at Jülich Supercomputing Centre (JSC). Additional computational time was granted by the state of Baden-Württemberg through bwHPC and the DFG (grant no. INST 39/963-1 FUGG, bwForCluster NEMO).

## Code availability

Classical MD simulations were performed using LAMMPS. (47) For visualization, pre- and post-processing we used OVITO, (48) ASE, (49) and matscipy. (50)




## Disclosure statement

No potential conflict of interest was reported by the author(s).

## Funding

We gratefully acknowledge funding by the DFG (Deutsche Forschungsgemeinschaft) within the SPP 2074 (Project No. 407714666).

## ORCID

Thomas Reichenbach  <http://orcid.org/0000-0001-7477-6248>  
 Stephan von Goedel  <http://orcid.org/0000-0002-4900-2184>  
 Stefan Peeters  <http://orcid.org/0000-0003-4612-7325>  
 Florian König  <http://orcid.org/0000-0002-4795-6451>  
 Georg Jacobs  <http://orcid.org/0000-0002-7564-288X>  
 Gianpietro Moras  <http://orcid.org/0000-0002-4623-2881>  
 Michael Moseler  <http://orcid.org/0000-0002-7064-1351>

## References

- Makinson, K. R. and Tabor, D. (1964), "Friction and Transfer of Polytetrafluoroethylene," *Nature*, **201**, pp 464–466. doi:10.1038/201464a0
- Anderson, W. J., Glenn, D. C., and Scibbe, H. W. (1968), "Friction Torque of Ball Bearings in Vacuum with Seven Polytetrafluoroethylene Composition Retainer Materials," *NASA-TN-D-4355*.
- Birkhofer, H. and Kümmerle, T. (2012), *Feststoffgeschmierte Wälzlager*, Springer: Berlin. doi:10.1007/978-3-642-16797-3
- Marquart, M., Wahl, M., Emrich, S., Zhang, G., Sauer, B., Kopnarski, M., and Wetzel, B. (2013), "Enhancing the Lifetime of MoS<sub>2</sub>-Lubricated Ball Bearings," *Wear*, **303**, pp 169–177. doi:10.1016/j.wear.2013.03.003
- Terwisscha-Dekker, H., Hogenelst, T., Bliem, R., Weber, B., and Bonn, D. (2023), "Why Teflon Is So Slippery While Other Polymers Are Not," *Physical Review E*, **107**, 024801. doi:10.1103/PhysRevE.107.024801
- Xu, Q., Tang, X., Zhang, J., Hu, Y., and Ma, T. (2023), "Unraveling Tribochemistry and Self-Lubrication Mechanism of Polytetrafluoroethylene by Reactive Coarse-Grained Molecular Dynamics Simulations," *ACS Applied Materials & Interfaces*, **15**, pp 45506–45515. doi:10.1021/acsami.3c10784
- von Goedel, S., Reichenbach, T., König, F., Mayrhofer, L., Moras, G., Jacobs, G., and Moseler, M. (2021), "A Combined Experimental and Atomistic Investigation of PTFE Double Transfer Film Formation and Lubrication in Rolling Point Contacts," *Tribology Letters*, **69**, 136. doi:10.1007/s11249-021-01508-9
- Biswas, S. K. and Vijayan, K. (1992), "Friction and Wear of PTFE—A Review," *Wear*, **158**, pp 193–211. doi:10.1016/0043-1648(92)90039-B
- Pooley, C. M. and Tabor, D. (1972), "Friction and Molecular Structure: The Behaviour of Some Thermoplastics," *Proceedings of the Royal Society of London. Series A, Mathematical and Physical Sciences*, **329**, pp 251–274. doi:10.1098/rspa.1972.0112
- Jang, I., Burris, D. L., Dickrell, P. L., Barry, P. R., Santos, C., Perry, S. S., Phillpot, S. R., Sinnott, S. B., and Sawyer, W. G. (2007), "Sliding Orientation Effects on the Tribological Properties of Polytetrafluoroethylene," *Journal of Applied Physics*, **102**, 123509. doi:10.1063/1.2821743
- Chiu, P. Y., Barry, P. R., Perry, S. S., Sawyer, W. G., Phillpot, S. R., and Sinnott, S. B. (2011), "Influence of the Molecular Level Structure of Polyethylene and Polytetrafluoroethylene on Their Tribological Response," *Tribology Letters*, **42**, pp 193–201. doi:10.1007/s11249-011-9763-0
- Pan, D., Fan, B., Qi, X., Yang, Y., and Hao, X. (2019), "Investigation of PTFE Tribological Properties Using Molecular Dynamics Simulation," *Tribology Letters*, **67**, 28. doi:10.1007/s11249-019-1141-3
- Mayrhofer, L., Moras, G., Mulakaluri, N., Rajagopalan, S., Stevens, P. A., and Moseler, M. (2016), "Fluorine-Terminated Diamond Surfaces as Dense Dipole Lattices: The Electrostatic Origin of Polar Hydrophobicity," *Journal of the American Chemical Society*, **138**, pp 4018–4028. doi:10.1021/jacs.5b04073
- Reichenbach, T., Mayrhofer, L., Kuwahara, T., Moseler, M., and Moras, G. (2020), "Steric Effects Control Dry Friction of H- and F-Terminated Carbon Surfaces," *ACS Applied Materials & Interfaces*, **12**, pp 8805–8816. doi:10.1021/acsami.9b18019
- Murray, J. S., Seybold, P. G., and Politzer, P. (2021), "The Many Faces of Fluorine: Some Noncovalent Interactions of Fluorine Compounds," *Journal of Chemical Thermodynamics*, **156**, 106382. doi:10.1016/j.jct.2020.106382
- Spyrakakis, F. and Dragani, T. A. (2023), "The EU's Per- and Polyfluoroalkyl Substances (PFAS) Ban: A Case of Policy over Science," *Toxics*, **11**, 721. doi:10.3390/toxics11090721
- Lu, X., Wong, K. C., Wong, P. C., Mitchell, K. A. R., Cotter, J., and Eadie, D. T. (2006), "Surface Characterization of Polytetrafluoroethylene (PTFE) Transfer Films during Rolling-Sliding Tribology Tests Using X-Ray Photoelectron Spectroscopy," *Wear*, **261**, pp 1155–1162. doi:10.1016/j.wear.2006.03.020
- Burris, D. L. and Sawyer, W. G. (2006), "A Low Friction and Ultra Low Wear Rate PEEK/PTFE Composite," *Wear*, **261**, pp 410–418. doi:10.1016/j.wear.2005.12.016
- Onodera, T., Nunoshige, J., Kawasaki, K., Adachi, K., Kurihara, K., and Kubo, M. (2017), "Structure and Function of Transfer Film Formed from PTFE/PEEK Polymer Blend," *The Journal of Physical Chemistry C*, **121**, pp 14589–14596. doi:10.1021/acs.jpcc.7b02860
- Simo Kanga, L., Nguyen, T.-D., Emrich, S., Oehler, M., Schmidt, T., Gedan-Smolka, M., Kopnarski, M., and Sauer, B. (2022), "The Effect of Irradiated PTFE on the Friction and Wear Behavior of Chemically Bonded PA46-PTFE-Cb and PA66-PTFE-Cb Compounds," *Wear*, **502–503**, 204380. doi:10.1016/j.wear.2022.204380
- Harris, K. L., Pitenis, A. A., Sawyer, W. G., Krick, B. A., Blackman, G. S., Kasprzak, D. J., and Junk, C. P. (2015), "PTFE Tribology and the Role of Mechanochemistry in the

- Development of Protective Surface Films,” *Macromolecules*, **48**, pp 3739–3745. doi:10.1021/acs.macromol.5b00452
- (22) Blanchet, T. A. and Kennedy, F. E. (1992), “Sliding Wear Mechanism of Polytetrafluoroethylene (PTFE) and PTFE Composites,” *Wear*, **153**, pp 229–243. doi:10.1016/0043-1648(92)90271-9
- (23) Tanaka, K. and Kawakami, S. (1982), “Effect of Various Fillers on the Friction and Wear of Polytetrafluoroethylene-Based Composites,” *Wear*, **79**, pp 221–234. doi:10.1016/0043-1648(82)90170-3
- (24) Lancaster, J. K. (1968), “The Effect of Carbon Fibre Reinforcement on the Friction and Wear of Polymers,” *Journal of Physics D: Applied Physics*, **1**, pp 549–559. doi:10.1088/0022-3727/1/5/303
- (25) Khedkar, J., Negulescu, I., and Meletis, E. I. (2002), “Sliding Wear Behavior of PTFE Composites,” *Wear*, **252**, pp 361–369. doi:10.1016/S0043-1648(01)00859-6
- (26) Fusaro, R. L. (1990), “Self-Lubricating Polymer Composites and Polymer Transfer Film Lubrication for Space Applications,” *Tribology International*, **23**, pp 105–122. doi:10.1016/0301-679X(90)90043-O
- (27) Cann, P. M., Spikes, H. A., and Hutchinson, J. (1996), “The Development of a Spacer Layer Imaging Method (SLIM) for Mapping Elastohydrodynamic Contacts,” *Tribology Transactions*, **39**, pp 915–921. doi:10.1080/10402009608983612
- (28) Fischer, D., Jacobs, G., Stratmann, A., and Burghardt, G. (2018), “Effect of Base Oil Type in Grease Composition on the Lubricating Film Formation in EHD Contacts,” *Lubricants*, **6**, 32. doi:10.3390/lubricants6020032
- (29) Fischer, D., Mues, H., Jacobs, G., and Stratmann, A. (2019), “Effect of over Rolling Frequency on the Film Formation in Grease Lubricated EHD Contacts under Starved Conditions,” *Lubricants*, **7**, 19. doi:10.3390/lubricants7020019
- (30) Hentschke, C. and Jacobs, G. (2013), *Untersuchung des Schmierfilmaufbaus und der Reibung bei dünnen Schmierfilmen mittels Interferometrie und FE8- Wälzlagerversuchen*, Abschlussbericht FVA 580-I, H. 1061, Forschungsvereinigung Antriebstechnik e.V.: Frankfurt.
- (31) Guegan, J., Kadiric, A., Gabelli, A., and Spikes, H. (2016), “The Relationship between Friction and Film Thickness in EHD Point Contacts in the Presence of Longitudinal Roughness,” *Tribology Letters*, **64**, 33. doi:10.1007/s11249-016-0768-6
- (32) Laukotka, E. M. (2007), *Referenzöle Datensammlung*, FVA H. Nr. 660 Forschungsvereinigung Antriebstechnik e.V.: Frankfurt.
- (33) Johnston, G. J., Wayte, R., and Spikes, H. A. (1991), “The Measurement and Study of Very Thin Lubricant Films in Concentrated Contacts,” *Tribology Transactions*, **34**, pp 187–194. doi:10.1080/10402009108982026
- (34) MacLaren, A., LaMascus, P., and Carpick, R. W. (2024), “Enhancing the Range and Reliability of the Spacer Layer Imaging Method,” *Tribology Letters*, **72**, 95. doi:10.1007/s11249-024-01890-0
- (35) Latorre, C. A., Ewen, J. P., Gattinoni, C., and Dini, D. (2019), “Simulating Surfactant–Iron Oxide Interfaces: From Density Functional Theory to Molecular Dynamics,” *The Journal of Physical Chemistry B*, **123**, pp 6870–6881. doi:10.1021/acs.jpcc.9b02925
- (36) Codrignani, A., Peeters, S., Holey, H., Stief, F., Savio, D., Pastewka, L., Moras, G., Falk, K., and Moseler, M. (2023), “Toward a Continuum Description of Lubrication in Highly Pressurized Nanometer-Wide Constrictions: The Importance of Accurate Slip Laws,” *Science Advances*, **9**, eadi2649. doi:10.1126/sciadv.adi2649
- (37) Frick, A., Sich, D., Heinrich, G., Stern, C., Gössi, M., and Tervoort, T. A. (2013), “Relationship between Structure and Mechanical Properties of Melt Processable PTFE: Influence of Molecular Weight and Comonomer Content,” *Macromolecular Materials and Engineering*, **298**, pp 954–966. doi:10.1002/mame.201200172
- (38) Brown, E. N., Trujillo, C. P., Gray, G. T., Rae, P. J., and Bourne, N. K. (2007), “Soft Recovery of Polytetrafluoroethylene Shocked through the Crystalline Phase II-III Transition,” *Journal of Applied Physics*, **101**, 024916. doi:10.1063/1.2424536
- (39) Watkins, E. K., and Jorgensen, W. L. (2001), “Perfluoroalkanes: Conformational Analysis and Liquid-State Properties from Ab Initio and Monte Carlo Calculations,” *The Journal of Physical Chemistry A*, **105**, pp 4118–4125. doi:10.1021/jp004071w
- (40) Pastewka, L., Moser, S., and Moseler, M. (2010), “Atomistic Insights into the Running-in, Lubrication, and Failure of Hydrogenated Diamond-Like Carbon Coatings,” *Tribology Letters*, **39**, pp 49–61. doi:10.1007/s11249-009-9566-8
- (41) Vafaei, S., Fischer, D., Jopen, M., Jacobs, G., König, F., and Weberskirch, R. (2021), “Investigation of Tribological Behavior of Lubricating Greases Composed of Different Bio-Based Polymer Thickeners,” *Lubricants*, **9**, 80. doi:10.3390/lubricants9080080
- (42) Ye, J., Sun, W., Zhang, Y., Liu, X., and Liu, K. (2018), “Measuring Evolution of Transfer Film–Substrate Interface Using Low Wear Alumina PTFE,” *Tribology Letters*, **66**, 100. doi:10.1007/s11249-018-1054-6
- (43) Uchiyama, Y. and Tanaka, K. (1980), “Wear Laws for Polytetrafluoroethylene,” *Wear*, **58**, pp 223–235. doi:10.1016/0043-1648(80)90152-0
- (44) Deulin, E. A., Mikhailov, V. P., Panfilov, Y. V., and Nevshupa, R. A. (2010), “Friction in Vacuum,” *Mechanics and Physics of Precise Vacuum Mechanisms*, pp 33–67, Springer: Dordrecht, Netherlands.
- (45) Brownell, M. and Nair, A. K. (2019), “Deformation Mechanisms of Polytetrafluoroethylene at the Nano- and Microscales,” *Physical Chemistry Chemical Physics*, **21**, pp 490–503. doi:10.1039/C8CP05111A
- (46) Jülich Supercomputing Centre JUWELS. (2019), “Modular Tier-0/1 Supercomputer at Jülich Supercomputing Centre,” *Journal of Large-Scale Research Facilities (JLSRF)*, **5**, A135. doi:10.17815/jlsrf-5-171
- (47) Thompson, A. P., Aktulga, H. M., Berger, R., Bolintineanu, D. S., Brown, W. M., Crozier, P. S., in ’t Veld, P. J., Kohlmeyer, A., Moore, S. G., Nguyen, T. D., Shan, R., Stevens, M. J., Tranchida, J., Trott, C., and Plimpton, S. J. (2022), “LAMMPS—A Flexible Simulation Tool for Particle-Based Materials Modeling at the Atomic, Meso, and Continuum Scales,” *Computer Physics Communications*, **271**, 108171. doi:10.1016/j.cpc.2021.108171
- (48) Stukowski, A. (2010), “Visualization and Analysis of Atomistic Simulation Data with OVITO—the Open Visualization Tool,” *Modelling and Simulation in Materials Science and Engineering*, **18**, 015012. doi:10.1088/0965-0393/18/1/015012
- (49) Larsen, A. H., Mortensen, J. J., Blomqvist, J., Castelli, I. E., Christensen, R., Dułak, M., Friis, J., Groves, M. N., Hammer, B., Hargus, C., Hermes, E. D., Jennings, P. C., Jensen, P. B., Kermode, J., Kitchin, J. R., Kolsbjerg, E. L., Kubal, J., Kaasbjerg, K., Lysgaard, S., Maronsson, J. B., Maxson, T., Olsen, T., Pastewka, L., Peterson, A., Rostgaard, C., Schiøtz, J., Schütt, O., Strange, M., Thygesen, K. S., Vegge, T., Vilhelmsen, L., Walter, M., Zeng, Z., and Jacobsen, K. W. (2017), “The Atomic Simulation Environment—A Python Library for Working with Atoms,” *Journal of Physics: Condensed Matter*, **29**, 273002. doi:10.1088/1361-648X/aa680e
- (50) Grigorev, P., Frérot, L., Birks, F., Gola, A., Golebiowski, J., Grieser, J., Hörmann, J. L., Klemenz, A., Moras, G., Nöhning, W. G., Oldenstaedt, J. A., Patel, P., Reichenbach, T., Rocke, T., Shenoy, L., Walter, M., Wengert, S., Zhang, L., Kermode, J. R., and Pastewka, L. (2024), “Matscipy: Materials Science at the Atomic Scale with Python,” *Journal of Open Source Software*, **9**, 5668. doi:10.21105/joss.05668